Biomedical Optics EXPRESS

Nanoparticle assisted photothermal deformation of individual neuronal organelles and cells

V. H. Romero,[1,2,6] Z. Kereselidze,[3,6] W. Egido,[4, 5] E. A. Michaelides,[4] F. Santamaria,[4] and X. G. Peralta[3,*]

[1]*Centro de Investigaciones en Optica A. C., Leon, Gto, 37150 Mexico*
[2]*Universidad de Guadalajara, División de Ciencias, Centro Universitario de Tonalá, Tonalá Jalisco 48525 Mexico*
[3]*Department of Physics and Astronomy, University of Texas at San Antonio, San Antonio, TX 78249 USA*
[4]*Department of Biology and Neurosciences Institute, University of Texas at San Antonio, San Antonio, TX 78249 USA*
[5]*Faculty of Medicine, Universidad Nacional Autonoma de Mexico, Mexico DF 07510 Mexico*
[6] *Equal contribution*
xomalin.peralta@utsa.edu

Abstract: Stimulation of the localized surface plasmon of metallic nanoparticles has been shown to be an effective mechanism to induce photothermal damage in biological tissues. However, few studies have focused on single cell or subcellular ablation. Our results show that, upon incubation, gold nanostars are internalized by neurons of acute mouse cerebellar brain slices, clustering inside or close to the nucleus. By stimulating the nanostars' surface plasmon using a femtosecond laser, we show deformation of single nuclei and single cells. Given its precision and extremely localized effect, this is a promising technique for photothermal therapy in areas sensitive to collateral thermal damage such as the nervous system.

OCIS codes: (170.1020) Ablation of tissue; (170.1530) Cell analysis; (240.6680) Surface plasmon; (160.4236) Nanomaterials.

References and links

1. M. Hu, J. Chen, Z.-Y. Li, L. Au, G. V. Hartland, X. Li, M. Marquez, and Y. Xia, "Gold nanostructures: engineering their plasmonic properties for biomedical applications," Chem. Soc. Rev. **35**(11), 1084–1094 (2006).
2. M. A. El-Sayed, "Some interesting properties of metals confined in time and nanometer space of different shapes," Acc. Chem. Res. **34**(4), 257–264 (2001).
3. B. Kang, M. A. Mackey, and M. A. El-Sayed, "Nuclear Targeting of Gold Nanoparticles in Cancer Cells Induces DNA Damage, Causing Cytokinesis Arrest and Apoptosis," J. Am. Chem. Soc. **132**(5), 1517–1519 (2010).
4. M. E. Wieder, D. C. Hone, M. J. Cook, M. M. Handsley, J. Gavrilovic, and D. A. Russell, "Intracellular photodynamic therapy with photosensitizer-nanoparticle conjugates: cancer therapy using a 'Trojan horse'," Photochem. Photobiol. Sci. **5**(8), 727–734 (2006).
5. A. Albanese, P. S. Tang, and W. C. W. Chan, "The Effect of Nanoparticle Size, Shape, and Surface Chemistry on Biological Systems," Annu. Rev. Biomed. Eng. **14**(1), 1–16 (2012).
6. L. Tong, Y. Zhao, T. B. Huff, M. N. Hansen, A. Wei, and J. X. Cheng, "Gold Nanorods Mediate Tumor Cell Death by Compromising Membrane Integrity," Adv. Mater. **19**(20), 3136–3141 (2007).
7. W. Lu, C. Xiong, G. Zhang, Q. Huang, R. Zhang, J. Z. Zhang, and C. Li, "Targeted photothermal ablation of murine melanomas with melanocyte-stimulating hormone analog-conjugated hollow gold nanospheres," Clin. Cancer Res. **15**(3), 876–886 (2009).
8. K. Jiang, D. A. Smith, and A. Pinchuk, "Size-Dependent Photothermal Conversion Efficiencies of Plasmonically Heated Gold Nanoparticles," J. Phys. Chem. C **117**(51), 27073–27080 (2013).
9. X. H. Huang, P. K. Jain, I. H. El-Sayed, and M. A. El-Sayed, "Gold nanoparticles: interesting optical properties and recent applications in cancer diagnostics and therapy," Nanomedicine (Lond) **2**(5), 681–693 (2007).
10. X. Huang, I. H. El-Sayed, W. Qian, and M. A. El-Sayed, "Cancer Cell Imaging and Photothermal Therapy in the Near-Infrared Region by Using Gold Nanorods," J. Am. Chem. Soc. **128**(6), 2115–2120 (2006).
11. V. K. Pustovalov, "Theoretical study of heating of spherical nanoparticle in media by short laser pulses," Chem. Phys. **308**(1-2), 103–108 (2005).

#217641 - $15.00 USD Received 30 Jul 2014; revised 19 Sep 2014; accepted 13 Oct 2014; published 20 Oct 2014

12. M. C. Daniel and D. Astruc, "Gold nanoparticles: Assembly, supramolecular chemistry, quantum-size-related properties, and applications toward biology, catalysis, and nanotechnology," Chem. Rev. **104**(1), 293–346 (2004).
13. X. H. Huang, I. H. El-Sayed, W. Qian, and M. A. El-Sayed, "Cancer cell imaging and photothermal therapy in the near-infrared region by using gold nanorods," J. Am. Chem. Soc. **128**(6), 2115–2120 (2006).
14. C. Loo, A. Lowery, N. J. Halas, J. West, and R. Drezek, "Immunotargeted nanoshells for integrated cancer imaging and therapy," Nano Lett. **5**(4), 709–711 (2005).
15. Z. Kereselidze, V. H. Romero, X. G. Peralta, and F. Santamaria, "Gold nanostar synthesis with a silver seed mediated growth method," J. Vis. Exp. **59**, 3570 (2012).
16. K. C. Mendoza, V. D. McLane, S. Kim, and J. D. Griffin, "Invitro application of gold nanoprobes in live neurons for phenotypical classification, connectivity assessment, and electrophysiological recording," Brain Res. **1325**, 19–27 (2010).
17. E. E. Connor, J. Mwamuka, A. Gole, C. J. Murphy, and M. D. Wyatt, "Gold nanoparticles are taken up by human cells but do not cause acute cytotoxicity," Small **1**(3), 325–327 (2005).
18. Y. F. Huang, K. Sefah, S. Bamrungsap, H. T. Chang, and W. Tan, "Selective photothermal therapy for mixed cancer cells using aptamer-conjugated nanorods," Langmuir **24**(20), 11860–11865 (2008).
19. L. C. Kennedy, L. R. Bickford, N. A. Lewinski, A. J. Coughlin, Y. Hu, E. S. Day, J. L. West, and R. A. Drezek, "A new era for cancer treatment: gold-nanoparticle-mediated thermal therapies," Small **7**(2), 169–183 (2011).
20. F. Santamaria, S. Wils, E. De Schutter, and G. J. Augustine, "The diffusional properties of dendrites depend on the density of dendritic spines," Eur. J. Neurosci. **34**(4), 561–568 (2011).
21. F. Santamaria, S. Wils, E. De Schutter, and G. J. Augustine, "Anomalous diffusion in Purkinje cell dendrites caused by spines," Neuron **52**(4), 635–648 (2006).
22. E. Hutter, S. Boridy, S. Labrecque, M. Lalancette-Hébert, J. Kriz, F. M. Winnik, and D. Maysinger, "Microglial response to gold nanoparticles," ACS Nano **4**(5), 2595–2606 (2010).
23. X. H. Huang, P. K. Jain, I. H. El-Sayed, and M. A. El-Sayed, "Plasmonic photothermal therapy (PPTT) using gold nanoparticles," Lasers Med. Sci. **23**(3), 217–228 (2008).
24. D. Missiakas, J. M. Betton, A. Chaffotte, P. Minard, and J. M. Yon, "Kinetic studies of the refolding of yeast phosphoglycerate kinase: comparison with the isolated engineered domains," Protein Sci. **1**(11), 1485–1493 (1992).
25. J. Ervin, E. Larios, S. Osváth, K. Schulten, and M. Gruebele, "What causes hyperfluorescence: folding intermediates or conformationally flexible native states?" Biophys. J. **83**(1), 473–483 (2002).
26. A. O. Govorov and H. H. Richardson, "Generating heat with metal nanoparticles," Nano Today **2**(1), 30–38 (2007).
27. H. H. Richardson, M. T. Carlson, P. J. Tandler, P. Hernandez, and A. O. Govorov, "Experimental and Theoretical Studies of Light-to-Heat Conversion and Collective Heating Effects in Metal Nanoparticle Solutions," Nano Lett. **9**(3), 1139–1146 (2009).
28. A. O. Govorov, W. Zhang, T. Skeini, H. Richardson, J. Lee, and N. A. Kotov, "Gold nanoparticle ensembles as heaters and actuators: melting and collective plasmon resonances," Nanoscale Res. Lett. **1**(1), 84–90 (2006).
29. S. Link and M. A. El-Sayed, "Shape and size dependence of radiative, non-radiative and photothermal properties of gold nanocrystals," Int. Rev. Phys. Chem. **19**(3), 409–453 (2000).
30. S. Link, C. Burda, B. Nikoobakht, and M. A. El-Sayed, "Laser-induced shape changes of colloidal gold nanorods using femtosecond and nanosecond laser pulses," J. Phys. Chem. B **104**(26), 6152–6163 (2000).
31. K. Salinas, Z. Kereselidze, F. DeLuna, X. G. Peralta, and F. Santamaria, "Transient extracellular application of gold nanostars increases hippocampal neuronal activity," J. Nanobiotechnology **12**(1), 31 (2014).
32. J. Chen, D. Wang, J. Xi, L. Au, A. Siekkinen, A. Warsen, Z.-Y. Li, H. Zhang, Y. Xia, and X. Li, "Immuno Gold Nanocages with Tailored Optical Properties for Targeted Photothermal Destruction of Cancer Cells," Nano Lett. **7**(5), 1318–1322 (2007).
33. D. O. Lapotko, E. Lukianova, and A. A. Oraevsky, "Selective laser nano-thermolysis of human leukemia cells with microbubbles generated around clusters of gold nanoparticles," Lasers Surg. Med. **38**(6), 631–642 (2006).

1. Introduction

There is a lot of interest in characterizing the bulk effects of nanoparticle mediated photothermal damage in tissues [1–4]. However, little is known about how this process takes place at the single cell and subcellular level [5, 6], partly because protocols to assess cell death or damage usually sample the tissue over periods of tens of minutes to hours. The basic principle behind photothermal therapy is to introduce nanoparticles with a surface plasmon resonance in the near-infrared (NIR) into cells and stimulating them with a laser. Since hemoglobin and water have the highest transmissivity in the NIR [7] this enables the stimulation of nanoparticles deeper into the tissue. When the nanoparticles are illuminated with laser light at a wavelength close to that of the surface plasmon, the electromagnetic energy absorbed heats up the electrons which thermalize with the lattice and the surrounding media [8, 9]. This transfer of thermal energy can affect the surrounding tissue in several ways.

#217641 - $15.00 USD Received 30 Jul 2014; revised 19 Sep 2014; accepted 13 Oct 2014; published 20 Oct 2014

Cell damage can occur from increasing the temperature a few degrees, causing cellular breakage and apoptosis, or it can lead to evaporation [10]. The details of the stimulation procedure, such as laser pulse duration and intensity, determine the mechanism and characteristics of the laser-particle interaction and the subsequent effects on the tissue [11]. To date, many procedures have been developed to functionalize nanoparticles so that they locate to specific cells [12–14]. By combining these schemes with nanoparticles engineered to have plasmon modes at a particular wavelength, we could develop highly localized photothermal therapies with minimal collateral damage. However, in order to achieve the goal of removing sick or damaged tissue at the single cell level it is necessary to first characterize the thermal effects and dynamics of nanoparticle stimulation at the cellular and subcellular levels.

In this study, we used a seed-mediated and silver-assisted growth method that we recently developed to obtain star shaped gold nanoparticles with a surface plasmon resonance in the NIR [15]. A two-photon microscope and the nanoparticle's luminescence were used to confirm that the nanoparticles were naturally internalized by neurons from acute mouse cerebellar brain slices [16, 17]. Using femtosecond pulsed NIR light we demonstrate single cell and single nucleus nanoparticle assisted destruction, we determined the energy threshold and temporal dynamics for this process in fixed and live neuronal tissues. Single cell control of photothermal therapies mediated by nanoparticles could offer significant advantages over present techniques that focus on bulk effects on tissues by reducing collateral damage in sensitive areas, such as the nervous system, and enabling nanoscale ablation capabilities [18, 19].

2. Methods

2.1 Gold nanostar synthesis and characterization

Gold nanostars were prepared using a modified seed-mediated growth process we recently published [15]. For the silver seed solution we prepared a 10 mL 0.25 mM solution of silver nitrate ($AgNO_3$) and stirred it with a stirring magnet. Separately we prepared a 10 mL 5 mM sodium citrate tribasic solution ($Na_3C_6H_5O_7$) and added 0.25 mL to the silver nitrate being stirred. Finally, we added 0.4 mL of a 40 mM $NaBH_4$ solution that had been previously chilled in a bucket with ice in the refrigerator for 15 min to the silver nitrate solution and continued stirring for another 5 min before removing the magnet. We kept this silver seed solution uncovered and in the dark until ready to use.

For the nanoparticle growth solution we prepared 10 mL of a 80 mM ascorbic acid solution ($C_6H_8O_6$) and 20 mL of a 50 mM cetyl trimethylammonium bromide solution ($C_{19}H_{42}BrN$), referred to as CTAB. The CTAB solution was immediately stirred with a stirring magnet on a warm plate at 30 °C. After CTAB had completely dissolved we turned off the heater but kept stirring. We then added enough silver nitrate solution to obtain a final molarity of 0.049 mM. After 1 min we added a concentrated solution of gold chloride ($HAuCl_4$) to a final molarity of 0.25 mM. After another minute we added 0.1 mL of the ascorbic acid solution. After 20 seconds we added 0.05 mL of the silver seed solution and continued stirring for 15 min. We then removed the magnet and kept the suspension at room temperature for 24 hours. After synthetizing the nanoparticles we washed them to remove the CTAB and other components. In all cases the initial volume was 10 mL and the final volume was 3 mL. The washing procedure consisted in sonicating the suspension for 2 minutes, then using the centrifuge for 5 min at 730 relative centrifugal force (rcf). This caused the nanoparticles to accumulate in the walls of the tube. We then removed the liquid with a pipette. We added DI water and sonicated for 2 more minutes, then used the centrifuge for 3 min at 460 rcf. We repeated this step, then centrifuged for 3 min at 380 rcf, removed the solution and added DI water to obtain a 3 mL suspension.

#217641 - $15.00 USD Received 30 Jul 2014; revised 19 Sep 2014; accepted 13 Oct 2014; published 20 Oct 2014

Absorption spectra of the prepared gold nanostar solutions were measured using a *Cary 14* UV/Vis/NIR Spectrophotometer. Scanning electron microscopy and energy-dispersive X-ray spectroscopy (EDS) analysis was performed in a FEG Hitachi S-5500 ultrahigh resolution electron microscope (0.4 nm at 30 kV).

2.2 Brain slice preparation and labelling

Sagittal cerebellar slices from 12 to 17 day old mice were prepared using standard procedures [20, 21] approved by the UTSA IACUC. The 200 μm thick slices were incubated for 30 min in artificial cerebro spinal fluid (aCSF) at 36 °C.

For fixed tissue studies, brain slices were then transferred to a chamber containing 1 mL of aCSF and 20 μL of $2x10^{-5}$ M gold nanostars for 1-3 hrs. In this step the particles were up taken by cells presumably through endocytosis [22]. Slices were washed in aCSF twice for 10 min to remove extracellular nanoparticles. Brain slices were then fixed by immersing them in 0.1 M phosphate buffered at 10% formalin (4% formaldeyhe) for 30 min and washed again in aCSF three times for 10 min. They were then transferred to a solution containing 1% sodium hydroxide in 80% alcohol for 5 min followed by 2 min in 70% alcohol and 2 min in distilled water. The slices were post-fixed in 0.06% potassium permanganate solution for 10 min and washed in distilled water for another 2 min. Finally, slices were transferred to a coverslip and mounted with a drop of 4', 6-diamidino-2-phenylindole (DAPI, Vector Laboratories, Burlingame, CA) for imaging purposes.

Live brain slices were incubated with a cytosolic fluorescent marker, cell tracker green CMFDA (Molecular Probes). Cell tracker was dissolved in DMSO (Sigma-Aldrich) at a concentration of 1 mM. Cerebellar slices were incubated in a 2 μM concentration of cell tracker in aCSF for 15 min at 37 °C. After that, slices were washed in aCSF twice for 10 min. Then the slices were incubated with 1 mL of aCSF and 20 μL of $2x10^{-5}$ M gold nanostars for 2 hours at room temperature. Finally, the slices were washed in aCSF twice for 10 min to remove extracellular nanoparticles and were imaged while in a room temperature circulating bath.

2.3 Imaging and laser excitation system

Images were collected using a Prairie Technologies two-photon laser scanning microscope (Madison, WI) with a 20x 0.9 N.A. water immersion objective (Olympus) coupled to a Coherent (Santa Rosa, CA) Chameleon tunable (700 – 950 nm) femtosecond (pulse duration <150 fs) Ti:sapphire laser with a 90 MHz repetition rate. Stacks of XY images were obtained at Z-steps between 0.1 and 1.0 μm up to a depth of 100 μm. Images were obtained at a rate of 0.02 – 0.45 frames/s with dwell times of 2-30 μs. Depending on the power output, the Ti:sapphire was used to generate only the luminescence from the gold nanostars and the two-photon fluorescence by DAPI (or cell-tracker), or both of those as well as exciting the surface plasmon of the gold nanoparticles. Two-photon excitation of DAPI and cell tracker was accomplished with wavelengths of 720 nm and 750-760 nm, respectively. The resulting fluorescence from the nuclei stained with DAPI or the cytosolic fluorescent marker was collected between 435 and 485 nm while, simultaneously, the luminescence from the nanoparticles was collected between 584 and 630 nm.

3. Results and analysis

3.1 Growth and internalization of nanostars

Scanning electron microscopy analysis shows well-formed star-shaped nanoparticles with the number of tips ranging from 7 to 10 and an average size of 190 ± 23 nm STD (standard deviation), see Fig. 1(a)-1(c). We confirmed that the nanoparticles were made of gold using EDS analysis (not shown). The absorption spectrum is broad and shows that the surface plasmon resonance is centered around 840 nm (Fig. 1(d)). Thus, our seed-mediated method

#217641 - $15.00 USD Received 30 Jul 2014; revised 19 Sep 2014; accepted 13 Oct 2014; published 20 Oct 2014

reliably generates a heterogeneous production of gold nanostars with a surface plasmon resonance in the NIR.

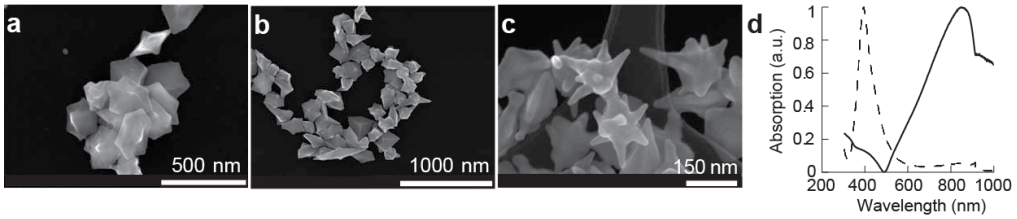

Fig. 1. Characterization of gold nanostars. (**a-c**) Scanning electron microscope images of gold nanostars. (**d**) Spectra of silver-seed (dashed) and gold nanostars (solid).

We imaged fixed brain slices that had been incubated with gold nanostars using a two-photon laser scanning microscope tuned to 720 nm in order to localize and quantify the internalization of gold nanostars by neurons. For imaging purposes, the fixation procedure included the staining of the nuclei with DAPI. During the imaging process, the fluorescent photons were separated into two different spectral windows, one for DAPI and the other for the expected two-photon luminescence of the nanoparticles [9] (see Methods). Initially, we collected 2D image stacks separated vertically between 0.1 and 0.2 μm for each channel and obtained 3D volumetric reconstructions of the viewing field by merging the images from the stacks. The volumetric reconstruction obtained from the spectral window corresponding to DAPI allowed us to locate the nuclei of the cells (Fig. 2(a)) and, by merging it with the data collected from the spectral window for the luminescence we were able to locate the nanoparticles (red dots, Fig. 2(b)). This analysis indicates that some nanoparticles are located close to the nuclei. By setting the transparency of the 3D reconstruction to 50%, we determined that nanoparticles also localize inside the nuclei (Fig. 2(c)). We quantified the number of cells that contained nanoparticles in their nuclei by focusing the microscope to an imaging plane where both nuclei and nanoparticles were visible. By collecting images in both channels and merging them (Fig. 3(a)-3(c)) we were able to count the number of nanoparticle containing nuclei within the first 100 μm from the surface of the slice. This analysis shows that 31 ± 4% SEM of cells contained nanoparticles in the nuclei (127 total cells counted in 13 samples). Since we can visualize the nuclei with DAPI, we focused on nanoparticle-containing nuclei for the surface plasmon stimulation experiments described in section 3.2.

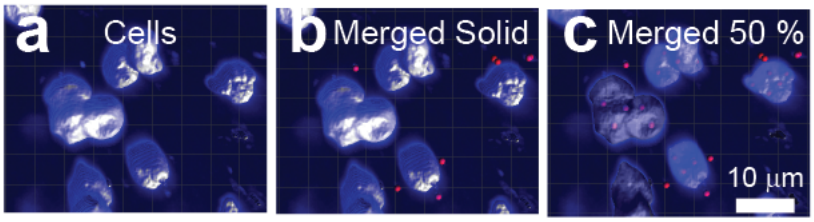

Fig. 2. Gold nanostars are located inside and around nuclei of fixed cerebellar neurons. (**a-c**) Volumetric reconstruction of the molecular layer of a cerebellar slice incubated with gold nanostars. (**a**) Reconstruction of the nucleus of 10 molecular layer neurons stained with DAPI. Images obtained from the channel filtered between 435 to 485 nm. (**b**) Identification of nanoparticle clusters (red dots) close to the nuclei. Image obtained by merging volumetric data from the two channels. (**c**) Same data as in (b) with the transparency of the reconstructed surfaces set to 50% showing the presence of nanoparticles inside the nuclei.

In order to estimate the size of the nanoparticle clusters localized inside the nuclei, we fitted a Gaussian along the intensity profile extracted from the image corresponding to the nanoparticle luminescence (Fig. 3(d)). In all cases, we centered the profile on the local intensity peak of the cluster. This analysis shows that the mean of the half-width-at-half-

#217641 - $15.00 USD Received 30 Jul 2014; revised 19 Sep 2014; accepted 13 Oct 2014; published 20 Oct 2014

maximum of the nanoparticle clusters is 0.34 ± 0.08 μm SEM (Fig. 3(e)). The diffraction limited waist at the focal point is w_r = 350 nm. The size calculated for the clusters is comparable to the diffraction limit of the microscope indicating that the cluster size is at the limit of resolution under these experimental conditions. However, we can estimate the maximum possible number of particles contained within the two-photon volume. Based on diffraction limit, the size of the two-photon volume can be calculated as $\pi^{3/2}$ $w_r^2 w_z$ assuming w_r = 350 nm and the spread along the z axis is w_z = 1.4 μm. Considering that the effective radius of a nanoparticle is ~100 nm then there would be a maximum number of ~200 nanoparticles within the two-photon volume. However, since the size of the cluster detected is comparable in size to the diffraction limit of the microscope we expect that each cluster actually contains a smaller number of nanoparticles.

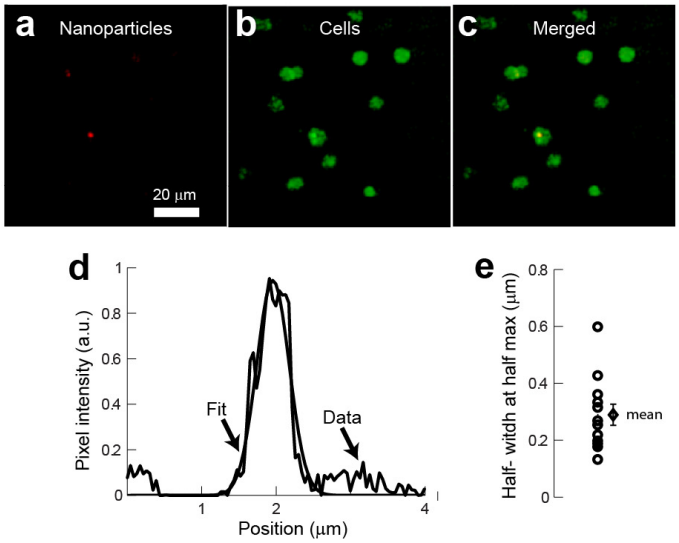

Fig. 3. Quantification of the nanoparticle clusters in fixed cerebellar slices. (**a-c**) clusters of nanoparticles were identified within nuclei located in the same imaging plane. (**a**) Luminescence from nanoparticle clusters obtained from the channel filtered between 584 to 630 nm. (**b**) Images of DAPI stained nuclei obtained from the channel filtered between 435 to 485 nm. (**c**) Merged image from the two channels. (**d**) Intensity profile of a cluster of nanoparticles and Gaussian fit. (**e**) Half-width-at-half-maximum obtained from the fits. Open circles were obtained from fits to different images and the rhomboid represents the mean ± SEM.

3.2 Surface plasmon stimulation results in deformation and destruction of organelles and neurons in fixed tissue

We characterized the effect of stimulating the surface plasmon of the nanoparticles by increasing the laser power as we collected images. A scanning wavelength of 720 nm allowed us to simultaneously excite the two-photon fluorescence of DAPI and the luminescence of the nanoparticles for imaging as well as stimulate the surface plasmon resonance of the particles. In general, we imaged with a laser power of 0.61 mW ± 0.06 SEM (n = 8 experiments, range 0.50 to 0.88 mW). Using the same procedure described in section 3.1 we located nanoparticle-containing nuclei after which we acquired up to 10 images at this low power of illumination before increasing the laser power to an average of 1.44 mW ± 0.12 SEM (range 1.04 to 1.75 mW) in order to stimulate the surface plasmon (Fig. 4(a)-4(c)). At each pixel the fluorescence intensity was collected for a period of time that varied from 2 to 30 μs, corresponding to the time during which that pixel was exposed to the laser's light. However,

#217641 - $15.00 USD Received 30 Jul 2014; revised 19 Sep 2014; accepted 13 Oct 2014; published 20 Oct 2014

it is important to note that in all of our experiments we used the scanning mode of the microscope therefore all the pixels within an image received the same amount of laser energy.

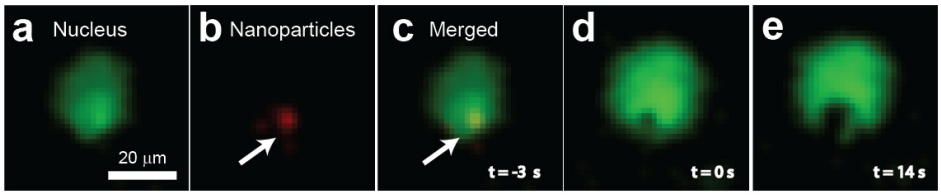

Fig. 4. Stimulation of the surface plasmon resonance at 720 nm causes loss of fluorescence and deformation of the nucleus in fixed tissues. (**a**) DAPI stained nucleus. (**b**) Luminescence showing a cluster of nanoparticles. (**c**) Merged images from the two channels. (**d-e**) Increasing the laser power from 0.88 to 1.55 mW produces a loss of fluorescence of a section of the nucleus (Media 1).

In some cases (n = 3 experiments) the increase in power resulted in the loss of fluorescence of an approximately circular area close to the nanoparticles (Fig. 4(d) and 4(e)). We characterized this area by locating the position of the nanoparticle cluster before increasing the power and measuring the distance of four points along the edge of the area with decreased fluorescence to the nanoparticle cluster's pre-stimulation position. On average, immediately after increasing the laser power, the area of loss of fluorescence had a radius of 1.26 μm ± 0.10 SEM (n = 7 clusters in 3 different experiments). In these experiments the increase in relative power was of 142% (range 75% to 244%) from a pre-stimulation power of 0.63 ± 0.12 mW SEM to a post-stimulation power of 1.44 ± 0.21 mW SEM. We continued to image the cells for up to 500 s at the high laser power. For all 7 clusters observed, the area of loss of fluorescence increased the most after the first exposure. After that initial increase the diameter of the diameter did not expand more than 4 μm. However, continuous monitoring of the image shows small changes in the nuclear shape. This observation suggests that the loss of fluorescence is not only due to a bleaching process but is also possibly due to an increase in the temperature of the nanoparticles which results in a region of photothermal damage surrounding them. In the experiment presented in Fig. 4 the center of the area that loses fluorescence is not in perfect register with the original nanoparticle location, possibly because of the scanning sequence of the laser, from top to bottom – left to right, and movement of the nucleus (see Media 1).

In other experiments (n = 5), the increase in power resulted in a continuous expansion and deformation of nanoparticle-containing nuclei (Fig. 5(a)-5(d)). In these experiments the pre-stimulation imaging power was 0.59 mW ± 0.07 SEM and the post-stimulation power was 1.43 mW ± 0.16 SEM with an increase in relative power of 146 ± 30% SEM. The efficiency of the photo deformation effect was calculated by counting the number of cells containing nanoparticles before increasing the laser power and those that showed deformation after increasing the laser power. This analysis shows that in 3 out of 5 experiments, all the nuclei which contained nanoparticles underwent a deformation while in the other two 50% of the nanoparticle-containing nuclei did. In general, the deformation followed a quasi-circular shape throughout the experiment, which is consistent with thermal effects (Fig. 5). We did not observe tissue deformation in any of the control experiments (no nanoparticles added) although we stimulated with the same light intensity (not shown). Furthermore, as is evident in Fig. 5, this deformation was restricted to nanoparticle-containing cells and therefore can be attributed to their presence within those cells.

The variability in the laser power needed to stimulate the surface plasmon mode can be attributed to two main factors. In contrast with most other studies found in the literature which use cell cultures [23], we are using 200 μm thick brain slices with cells and nuclei located at different depths. The deeper a nucleus is in a tissue, the more photons are scattered

#217641 - $15.00 USD Received 30 Jul 2014; revised 19 Sep 2014; accepted 13 Oct 2014; published 20 Oct 2014

and the more uniform the thermal dissipation and tissue tension. In addition there is variability in the depth at which the nanoparticles are located and in the number of nanoparticles within a cluster, both of which influence the efficiency of plasmon excitation. These factors directly impact our ability to determine a clear threshold to initiate damage. To overcome this limitation we performed experiments in which we 1) visualized the nanoparticles in the cells, 2) imaged with increasing power steps until we saw ablation damage in the tissue, 3) moved to a different part of the same slice at a similar depth and applied the energy increase that was previously determined to cause damage. This procedure assures the use of the minimal energy necessary to elicit deformation of the cells.

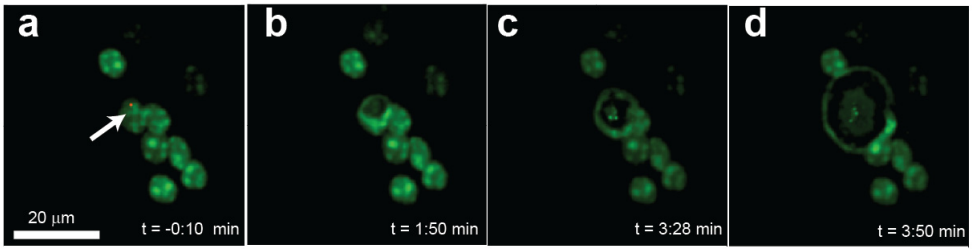

Fig. 5. Photoassisted morphological deformation of a single fixed cell containing gold nanostars. (**a**) Image of 8 nuclei in which only one cell contains nanoparticles, indicated by the arrow. (**b-d**) Temporal sequence collected after increasing the imaging laser power from 0.80 to 1.9 mW with an imaging wavelength of 752 nm.

As we did previously, we characterized the area affected by the plasmon stimulation by locating the position of the nanoparticle cluster before stimulation and measuring the distance of four points along the edge of the area with decreased fluorescence to the nanoparticle cluster's pre-stimulation position. In most experiments, the perimeter of the area with decreased fluorescence quickly merged with the edge of the deformed nucleus (Fig. 5(b)-5(c)). We defined the maximum radius of expansion when this expanding edge either left the imaging area or fused with another nucleus (about 300 s). Plots of the radius of the area of deformation as a function of time show a continuous increase in the radii in all cases (Fig. 6(a)). By plotting the normalized radius (change in radius divided by the maximum radius achieved) as a function of time we found that the cells needed to be exposed for about 100 s (10 frames) in order to reach 50% of the maximum radius of expansion (Fig. 6(b)). The maximum diameter of expansion directly correlates with the relative change in laser power (Fig. 6(c)) which is also consistent with a photothermal process being responsible for the deformation. The area of decreased fluorescence stopped increasing in size after irradiation ended.

The deformation observed is the result of the electromagnetic radiation absorbed by the nanoparticle during the exposure time dissipating into heat for a time that corresponds to the exposure time plus the time between frames (2.2 s for 0.45 frames/s). In the first set of experiments described above we found that the average radius right after increasing the laser power was 1.26 μm. Assuming we have the same rate of electromagnetic energy dissipation into heat in subsequent exposures, we would expect to see a linear increase in the radius as the number of frames collected increases. That is ten times the average radius for ten frames (~12.6 μm), which is in agreement with the results shown in Fig. 6. This cumulative effect implies that the nanoparticles do not melt or vaporize during the irradiation.

#217641 - $15.00 USD Received 30 Jul 2014; revised 19 Sep 2014; accepted 13 Oct 2014; published 20 Oct 2014

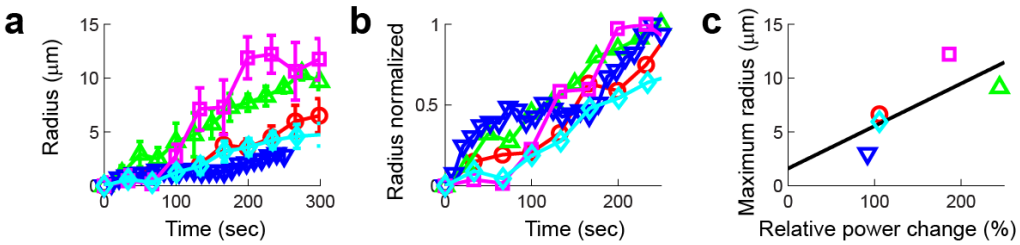

Fig. 6. Expansion of neuronal nuclei after excitation of the surface plasmon of gold nanostars. (**a**) Radius of the area of decreased fluorescence around the nanoparticle as a function of time for 5 different cells. (**b**) Normalized radius as a function of time for the same experiments shown in (a). (**c**) Maximum radius of expansion achieved with different relative changes in laser power.

3.3 Surface plasmon stimulation results in deformation and destruction of live neurons

We wanted to determine if nanoparticles were present in live cells. In this case we could not use DAPI to stain the nucleus so we used a cytosolic marker instead. Therefore, the resulting images show the fluorescent signal of the cytosol with a dark nucleus. Using the same volumetric reconstruction techniques described in Fig. 2 (data no shown), we located nanoparticle-containing cells by separating the fluorescent photons into two spectral windows, one for the cytosolic marker and the other for the luminescence of the nanoparticles, and merging them. We found that the nanoparticles were located close to the nucleus (Fig. 7(a)), confirming our results from fixed tissue. By increasing the laser power, we stimulated the surface plasmon of nanoparticle-contaning cells and performed a total of 8 experiments, one of which did not show visible effects due to the surface plasmon stimulation. In the other seven, when we stimulated the surface plasmon we observed that there was a destruction of the cytosol which originated at the nanoparticle cluster's location (Fig. 7(b)-7(d)). From 17 cells counted in 8 samples, 7 were destroyed due to surface plasmon stimulation. The destruction of the cytosol appears as a breakdown of the fluorescent marker attached to the proteins resulting in a region of increased fluorescence in Fig. 7. It can be ascribed to thermally induced protein denaturation [24, 25]. In the experiment reported in Fig. 7 the damage appears to initiate from only one of the two visible nanoparticle clusters, possibly the one that is located closer to the focus of the laser. At later times, Fig. 7(d), other nanoparticles came into focus, possibly due to movement of the cellular material. Destruction of the cytosol eventually reaches the nucleus and starts to degrade the cellular membrane (Media 2). In general, for the live cell experiments, we had to use higher laser powers both for imaging and to destroy the cells compared to the fixed tissue experiments, possibly due to the bath reducing the power delivered to the cells and its constant circulation which has a cooling effect. The mean pre-stimulation laser power was 1.61 ± 0.30 mW SEM, and the post-stimulation was 3.59 ± 0.27 mW SEM, with a relative change in power of 154 ± 29%. In cases in which there were a large number of nanoparticles in the tissue, the surface plasmon stimulation resulted in the deformation and destruction of most of the cells within the viewing area (not shown). The area of increased fluorescence stopped increasing in size after irradiation ended. We did not observe tissue deformation in any of the control experiments (no nanoparticles added) although we stimulated with the same light intensity.

#217641 - $15.00 USD Received 30 Jul 2014; revised 19 Sep 2014; accepted 13 Oct 2014; published 20 Oct 2014

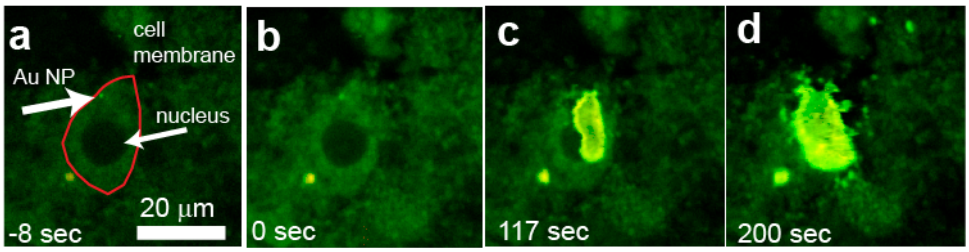

Fig. 7. Single cell ablation in live cells. The sequence of images shows a Purkinje cell containing nanoparticles imaged (**a**) before an (**b-d**) after increasing the laser power (from 1.37 to 4.06 mW). The thermal expansion remained contained within the cell body (Media 2). The line in (a) locates the cell boundary.

4. Discussion

The current understanding of nanoparticle assisted photothermal ablation is that when metallic nanoparticles are illuminated with a wavelength close to their localized surface plasmon resonance, the nanoparticles absorb the photon energy and effectively become heat generators by virtue of having hot electrons thermalizing with the lattice through electron-phonon interactions [26]. The thermal energy is also transferred to the surrounding media through phonon-phonon interactions and results in the thermal effects observed [8]. The collective effect of exciting the surface plasmon using light and resulting in an increase in temperature of the surrounding media is known as light-to-heat conversion [27]. The efficiency of the light-to-heat conversion process depends on stimulation of the plasmon mode by absorption of the electromagnetic radiation and the thermodynamic processes that control the heat transfer between the particle and the surrounding medium [11, 28, 29].

In order to obtain an estimate of the increase in temperature of the neurons, it is necessary to consider the relationship between the different characteristic times for thermal diffusion involved [11]. The time required for a gold nanosphere to reach thermal equilibrium is $t_o \sim r_o^2 \rho_o c_o/(4k_o)$ = 20 ps where ρ_o, c_o and k_o are the density, specific heat and thermal conductivity of gold, and the radius of the nanoparticles is r_o = 100 nm. Achieving thermal equilibrium is much slower than the laser pulse duration (t_p = 150 fs), therefore, the gold nanoparticle does not reach a homogeneous temperature within a single pulse. However, given that the interval between pulses is ~10 ns, the nanoparticles reach a homogeneous internal temperature before the arrival of the next pulse. In addition, the laser power used for plasmon stimulation is smaller than that used to melt gold nanoparticles using femtosecond pulses (0.01 J cm^{-2}) [30], therefore we are certain that we are not modifying the nanoparticles' shape during the experiments. Similarly, the gold nanosphere-to-surrounding media characteristic time constant to reach thermal equilibrium is $t_T \sim r_o^2 \rho_m c_m/(4k_m)$ = 16 ns, where r_o is the nanoparticle radius, ρ_m, c_m and k_m are the density, specific heat and thermal conductivity of the surrounding medium. Thus, there is almost no exchange of heat between the nanoparticle and the environment during a pulse and given that the inter pulse interval is ~10 ns, the nanoparticle does not thermalize with the environment between pulses. The characteristic time for the nanoparticle to cool down is $t_c \sim r_o^2 \rho_o c_o/(3k_m)$ = 14 ns which is comparable to the inter pulse interval. This analysis and the cumulative effect observed in our experiments indicates that in order to estimate the increase in temperature of the neurons it is necessary to consider the effect of a train of laser pulses. Following [11], let's assume, a total exposure time of 30 μs and a spot size of 350 nm. If the particle cools down in between pulses then irradiating a 100 nm radius gold nanosphere with an average power of 0.6 mW causes an increase of only 3.7 K. This is consistent with our results in which no deformation was observed. If instead we consider an average power of 1.5 mW then this results in an increase of the nanoparticles' surface temperature by 9.3 K. This calculation is for a single

#217641 - $15.00 USD Received 30 Jul 2014; revised 19 Sep 2014; accepted 13 Oct 2014; published 20 Oct 2014

nanoparticle, however, having clusters of nanoparticles can result in higher temperature increases [25]. Therefore, our surface plasmon resonance stimulation could increase the temperature of the tissue to above 40 °C, assuming a room temperature of 23 °C causing protein denaturation but no evaporation of the tissue. Given that this is a modest temperature increase, we believe the temperature of the cells decreases to pre-stimulation values after irradiation has stopped.

The results presented in this paper are relevant both in the context of nanoparticle assisted photothermal therapy as well as demonstrating that, for low laser powers, two-photon microscopic imaging of nanoparticle containing cells can be used for studies of the non-lethal effect of nanoparticles on cell function [31]. A majority of other studies on nanoparticle assisted photothermal therapy use cell cultures instead of brain slices [23]. This translates into more controlled and reproducible irradiation conditions at the expense of having conditions that are closer to those in real tissue. In addition, the laser parameters used for stimulation, such as pulse duration and repetition rate, are related to the characteristics of the laser-particle interaction and the subsequent effects on the tissue [11]. Both of these variables affect our ability to make a direct comparison of the laser energies used between the different studies found in the literature.

5. Conclusion

We have shown that gold nanostars are readily internalized by cerebellar neurons and that the nanoparticles localize close or inside the nucleus. We were able to image the tissue, the luminescence of the nanoparticles, and stimulate their surface plasmon simultaneously in fixed and live preparations. The energy delivered and exposure time can be regulated to destroy only a section of the nucleus or the entire cell. The thermally induced destruction of cells shown in this study lies between thermally induced cell death and full vaporization of cells [3, 32, 33]. Nanoparticle assisted photothermal therapy is especially promising for ablating single cells in areas sensitive to collateral thermal damage, such as the nervous system, and can be highly precise even at the single organelle level. Given its precision and extremely localized effect, this method could be of great value in basic and applied applications to probe neuronal function as well as nervous system development.

Acknowledgments

This project was supported by the National Institute on Minority Health and Health Disparities RCMI G12MD007591 from the National Institutes of Health and the NSF PREM DMR 0934218.

#217641 - $15.00 USD Received 30 Jul 2014; revised 19 Sep 2014; accepted 13 Oct 2014; published 20 Oct 2014